Experimental investigation on the effect of forward-facing steps and gaps combined with wall suction on boundary layer transition

Jeanne Methel, Maxime Forte, Olivier Vermeersch, Grégoire Casalis

Experimental investigation on the effect of forward-facing steps and gaps combined with wall suction on boundary layer transition

Jeanne Methel[1*], Maxime Forte[1*], Olivier Vermeersch[1] and Grégoire Casalis[2]

[1*]ONERA/DMPE, Université de Toulouse, Toulouse, 31055, France.

[2]ISAE-SUPAERO, Université de Toulouse, Toulouse, 31055, France.

*Corresponding author(s). E-mail(s): jeanne.methel@onera.fr; maxime.forte@onera.fr;
Contributing authors: olivier.vermeersch@onera.fr; gregoire.casalis@isae-supaero.fr;

Abstract

Wall suction is known to be an effective Laminar Flow Control (LFC) technique to delay laminar-turbulent transition, but its commercial implementation is still limited due to design and integration issues. In particular, current design tools that model wall suction do not account for potential surface discontinuities that can arise during installation. However, these defects should be accounted for since they generally move transition further upstream, which could cancel drag reduction benefits from wall suction. Given this context, the present investigation aims at experimentally characterizing the combined effect of wall suction and two types of surface defects that can be found on aerodynamic surfaces, i.e., forward-facing steps (FFS) and gaps. Critical relative dimensions (at which transition occurs at the defect location) were different for each type of defect but remained unchanged regardless of whether wall suction was applied or not. For subcritical defects (defects where transition occurs further downstream of their location), wall suction could still delay transition, with reduced effectiveness. Spectral analysis inside the boundary layer revealed that the transition mechanism, governed by Tollmien-Schlichting instabilities, was unchanged in the presence of either

critical or subcritical defects. The resulting increase in amplification of the existing instabilities due to either defect warranted the use of the $\boldsymbol{\Delta N}$ model to capture this effect. Wall suction is therefore a robust LFC technique that can compete with the destabilizing effects of subcritical defects, albeit less effectively than in a smooth configuration. However, given the chosen suction flow rates, this technique could not delay or prevent the critical dimensions determined for cases without suction.

Keywords: laminar-turbulent transition, boundary layer suction, Laminar Flow Control, surface defects, gaps, forward-facing steps, Tollmien-Schlichting instabilities

1 Introduction

Renewed interest in laminar flow research is emerging to face both economic and environmental concerns to reduce aviation's fuel consumption. The purpose of such research is to reduce skin-friction drag by maximizing the region of laminar flow through laminar-turbulent transition delay. One approach is through Laminar Flow Control (LFC), which consists in implementing additional technology to maintain a laminar boundary layer over the entire profile.

In particular, one such LFC method to delay transition is wall suction. For a two-dimensional flow, such as the one in the present study, laminar-turbulent transition is governed by viscous instabilities, i.e., Tollmien-Schlichting (TS) instabilities. For this type of flow, these TS instabilities can also be referred to as primary instabilities. As shown by Saric et al (2011) and Reed et al (1996), the growth of TS instabilities can be attenuated (thereby increasing flow stability) by making the boundary layer's mean velocity profile curvature, $\mathrm{d}^2U/\mathrm{d}y^2$, more negative. This stabilizing effect can be successfully achieved through wall suction, which introduces a normal component of velocity at the wall, and redistributes the disturbance energy closer to the wall, where higher dissipation occurs (Reynolds and Saric (1986)).

Extensive literature reviews by Braslow (1999), Joslin (1998) or Krishnan et al (2017) attest to the proven effectiveness of wall suction, starting back as early as in the 1950s. However, some of the main obstacles to its more widespread implementation are related to practical considerations, such as properly assessing the impact of surface discontinuities that can arise during manufacturing or operation on the performance of a wall suction system (Arnal and Archambaud (2008)).

In general, surface defects over solid surfaces are known to destabilize the boundary layer, and therefore promote the onset of a premature laminar-turbulent transition. In an early attempt to avoid critical defects (where transition would occur at the defect location), Nenni and Gluyas (1966) determined transition criteria that should not be exceeded: these Reynolds numbers

were based on the freestream velocity and the defect dimensions. These dimensions correspond to height for backward- and forward-facing steps, BFS and FFS respectively, and streamwise length for gaps. Later studies (Béguet et al (2016) and Costantini et al (2015)) suggested using local flow properties and relative defect dimensions with respect to the local boundary layer thickness instead; however, use of Nenni and Gluyas criteria can still be found today because of its simplicity, a decisive factor of usability in the aerospace industry. Since then, numerous investigations, both experimental (e.g., Klebanoff and Tidstrom (1972), Dovgal et al (1994), Wang and Gaster (2005) or Rius-Vidales and Kotsonis (2020)) and numerical (e.g., Perraud et al (2005), Rizzetta and Visbal (2014) or Lüdeke and Backhaus (2018)) were carried out to further understand the physics involved in the onset of laminar-turbulent transition induced by surface defects. However, the complexity of most numerical models does not currently allow to consider this approach as part of the design process.

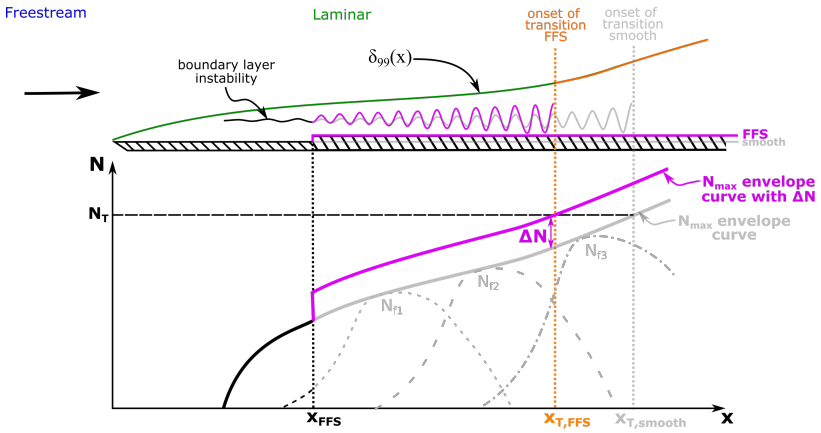

Fig. 1 Schematic representation of boundary layer transition over a flat plate (top) and the spatial evolution of N factor curves for three frequencies and their maximum envelope curve without and with the effect of the forward-facing step through the ΔN shift (bottom).

One relatively simple but effective approach to modeling the effect of a surface defect on transition is to use the ΔN approach, schematically shown in Figure 1. The first step consists in applying the e^N method and determining the threshold N_T value at which transition occurs on a smooth surface. Simultaneously developed by Van Ingen (1956) and Smith and Gamberoni (1956), the principle behind the e^N method is to use linear stability theory (LST) to evaluate the spatial amplification rates of primary instabilities in the laminar region (here, TS instabilities) at given frequencies. Spatial integration of these amplification rates results in N factor curves for each frequency, for example shown as N_{f1}, N_{f2} and N_{f3} on Figure 1 for three different frequencies. Based on these individual N factor curves, a maximum N factor envelope curve can be evaluated. This curve constitutes the basis of the e^N method: the location

where the envelope curve's value exceeds a threshold N_T value corresponds to the transition position.

Once the smooth surface configuration is established, the next step is to extend the e^N method to cases with surface defects. The maximum N factor envelope curve for the smooth configuration is artificially shifted by a ΔN, starting at the location of the defect, as shown on Figure 1. The value of the ΔN is determined by the surface defect characteristics and flow properties. This ΔN method was most successfully introduced in studies by Wang and Gaster (2005) or Crouch et al (2006), in which no wall suction was present. In terms of physics, the presence of the defect is assumed to induce an amplification boost in the already existing flow instabilities. The effect of the surface defect is therefore to move the transition position, since the shift in ΔN will also change the location at which the now fixed value of N_T is reached. Empirical models, based on experimentally-determined transition positions and LST calculations, are currently most commonly used. This approach was shown to successfully capture the effect of FFS in both numerical and experimental studies, such as Edelmann and Rist (2015) or Crouch and Kosorygin (2020). However, these models are all based on the cases without suction: a need therefore still exists to determine if the competing effects of wall suction and surface defects can still be captured by the ΔN approach.

Despite the generally destabilizing effect of surface defects, wall suction through micro-perforated metallic panels was successfully implemented on aircraft and flight tested in the 1980s in France (e.g., to further understand the interaction between surface defects and suction, Bulgubure and Arnal (1992)), and the 1990s in the United States (e.g., Maddalon (1991)). Discrepancies between predicted and experimental data were, however, considered too significant to validate the existing design tools. For this reason, along with high costs and bulkiness, no commercial implementation ensued. In an effort to improve models, numerical studies, such as by Hahn and Pfenninger (1973), Al-Maaitah et al (1989), or more recently Zahn and Rist (2018), were conducted to improve understanding of the interaction between surface defects and suction.

With a similar purpose, the present study seeks to provide further experimental data and analysis on the combined effect of wall suction and two model surface defects representative of those found on aerodynamic surfaces: FFS and gaps. This investigation is a continuation of the previously published experimental results on wall suction and wires. All details on the experimental facility and method used to conduct the present study can therefore be found in Methel et al (2019). However, a brief review of the experimental facility is first provided, along with the reference configuration, where the effects of wall suction on a smooth (no defect) flat plate are presented. Then, the FFS and gaps are introduced, and three facets of their effect combined with wall suction are analyzed: mean flow and transition position, transition mechanisms, and modeling using the ΔN method.

2 Overview of the experimental method

In the following section, a brief review of the experimental facility is presented, along with previously published results of the smooth configuration with different wall suction distribution to provide a reference for later results. Additional details can be found in Methel et al (2019).

2.1 Experimental facility

The experimental facility used in this study is the ONERA TRIN 2 subsonic wind tunnel, which operates at local atmospheric conditions. Although test section velocities range from 20 m.s^{-1} to 50 m.s^{-1} (approximately corresponding to unit Reynolds numbers of $1 \cdot 10^6$ m^{-1} and $3 \cdot 10^6$ m^{-1}), all measurements for this study were acquired at a single nominal unit Reynolds number of $2.6 \cdot 10^6$ m^{-1} ($\sim$40 m.s^{-1}). The unit Reynolds number, $\frac{\rho U_\infty}{\mu}$, is based on the ambient air density ρ and dynamic viscosity μ, and the freestream velocity U_∞ at the entrance of the test section.

This facility was adjusted for laminar-turbulent transition experiments by including a noise-reduction chamber to separate the test section from the driving fan. The purpose of this chamber is to prevent the propagation of pressure waves from the fan into the test section. To achieve this effect, the walls, floor and ceiling of the chamber are lined with foam, and a partition forces the flow path into a U between the diverging nozzle and the fan to create an additional obstacle. As a result, the maximum freestream turbulence levels, evaluated over frequencies ranging from 3 Hz to 10 kHz, across all tested speeds were below 0.18%. More details on the evaluation of the turbulence levels can be found in Methel et al (2018).

The three main types of measurements performed in this study were: static pressure, to establish a zero pressure gradient over the flat section of the flat plate and to provide a reference input for subsequent boundary layer calculations; flow rate, to control wall suction distribution; and flow velocity, to evaluate the mean and fluctuation components of streamwise velocity in the boundary layer. Flow velocity was measured using constant temperature anemometry with a Dantec Streamline, a 90C10 CTA module and a 55P15 probe, mounted on a two-dimensional traverse. For each data point, 400 000 samples were acquired at a frequency of 25 kHz. The hotwire probes were calibration in situ at the start and end of each test.

The model mounted in the test section was a flat plate with a leading edge that was designed using numerical optimization to minimize the suction peak velocity, in a similar approach to that described by Fransson (2004) or Corelli Grappadelli et al (2021). The flat plate spanned the entire width of the test section (0.4 m) and had a total length of 1.10 m. The suction region, located 0.18 m from the leading edge, was divided in nine suction chambers that were each 0.048 m (x) long by 0.019 m (y) deep and separated by 0.002 m (x) stringers. The chamber labeled C1 was located closest to the leading edge and C9 furthest downstream. Figure 2 gives an overview of the main features

of the flat plate, along with the location of the surface defects, which will be discussed later.

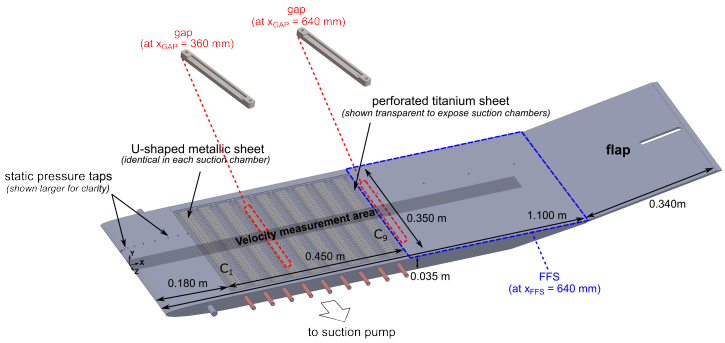

Fig. 2 General layout of the flat plate and flap with details on the suction region and surface defects.

To achieve as close as possible to a Blasius flow on the upper side of the model, the flat plate and flap incidences were set to 0.08 and 3.5 degrees respectively (positive angle is pitching down). This set-up resulted in a zero pressure gradient over the entire length of the plate, except in the leading egde region. Additionally, the presence of two dimensional flow over the velocity measurement area was verified. Given these flow conditions combined with the relatively low freestream turbulence levels in the test section, transition is expected to occur as a result of the linear amplification of primary modes, i.e., to follow the traditional path for low disturbance flows, as defined by Morkovin et al (1994).

This transition scenario was confirmed experimentally, as shown in Figure 3. The profiles in this figure are located at the streamwise position x equal to 558 mm from the leading edge, with a solid panel over the suction region. This position was chosen close to the onset of transition (located at x equal to 740 mm, equivalent to a transition Reynolds number of $1.92{\cdot}10^6$) such that the TS instabilities would be sufficiently amplified to be identified, as shown on Figure 3(b). To obtain the experimental profile, the velocity sprectrum of each point in the profile of Figure 3(a) was integrated over a narrow range of frequencies, in the present case between 592 Hz and 632 Hz. The experimental profile is then compared with the eigenfunction of the streamwise velocity fluctuations at 600 Hz, calculated with LST. This 600 Hz frequency value was chosen based on the e^N method as illustrated on Figure 4: the experimental transition position is reported on the maximum N envelope curve (labeled N_{max}) to determine the frequency that is most amplified at this location, and the corresponding transition N_T, in the present case equal to 6.2. Such an N_T value is agreement with previous transition studies performed in the same wind tunnel facility (Studer et al (2006)).

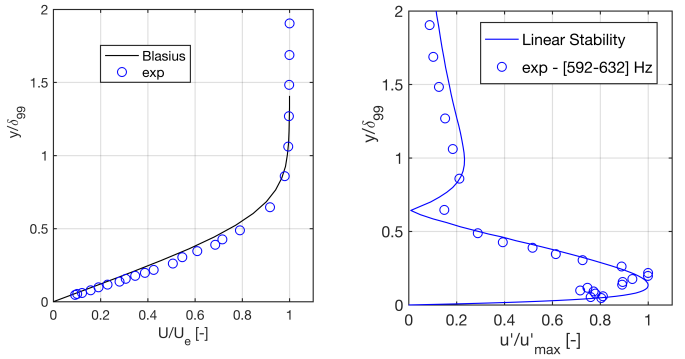

(a) Normalized mean velocity profile.

(b) Normalized fluctuating velocity profile at ∼600 Hz.

Fig. 3 Streamwise mean and fluctuating velocity profiles at $x = 558$ mm and $\delta_{99} = 2.43$ mm at operating Re $= 2.6 \cdot 10^6$ m^{-1}.

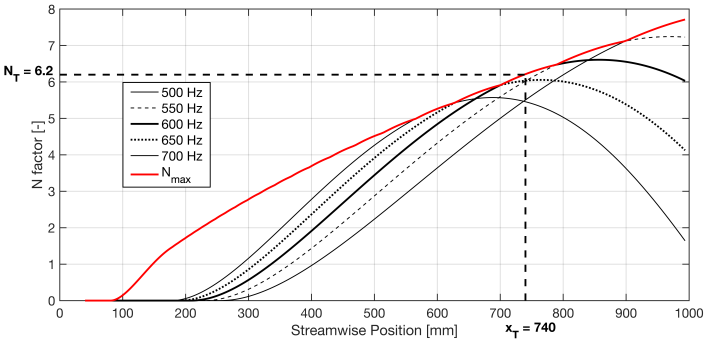

Fig. 4 Calculated N-factor evolution using LST for reference Blasius flow (based on experimental data) at operating Re $= 2.6 \cdot 10^6$ m^{-1}.

2.2 Reference configuration: wall suction on smooth flat plate

Although the results from this section have already published in Methel et al (2019), a brief summary is provided as a reminder of the reference smooth (no defects) configuration. The suction region was divided into nine independent suction chambers, and was sealed with a 0.9 mm-thick micro-perforated titanium sheet. This suction panel (referred to as P2 in Methel et al (2019)) had 90 μm diameter perforations that were evenly space in a square pattern of dimensions 1.6 mm by 1.6 mm, thereby having a porosity p of approximately 0.26% (with porosity defined as the ratio of the open area to the total surface of the panel). Each suction chamber was connected to its corresponding mass flow meter-controller, and the total mass flow rate was kept constant at 0.4 g.s^{-1} while only suction distribution changed between each case. This suction flow rate was chosen for two main reasons: first, to enable comparison

with previous (unpublished) ONERA studies performed on the same experimental set-up; and then, such flow rates delayed transition, with respect to the *no suction* configuration, to positions along the flat plate that could still be measured. Next, different spatial distributions of wall suction were chosen to investigate how boundary layers having undergone stabilization at different stages of its development respond to surface defects.

The four chosen suction configurations were: *no suction*, where the porous panel was mounted over the suction region but the valves of the mass flow meters were shut; C1/0.400, where all 0.4 $g.s^{-1}$ of suction were concentrated on chamber C1; C3,5/0.200, where suction was split in 0.2 $g.s^{-1}$ over chambers C3 and C5; and finally, *full suction*, where suction was equally distributed across all chambers (resulting in 0.044 $g.s^{-1}$ per chamber). With each suction chamber having a designated mass flow meter, the mass flow rate in each chamber was constantly monitored to ensure that the flow was distributed according to the chosen configuration. To prevent any passive suction or blowing, chambers without suction had flow meters with shut valves.

The transition position was defined as the location where the streamwise velocity fluctuations u_{RMS} start to increase past a threshold gradient value (explained in more details in Methel et al (2019)).Physically, this initial rise in streamwise velocity fluctuations is directly related to the onset of the first turbulent spots that arise because the TS instabilities in the boundary layer reach a threshold amplification (which corresponds to the N_T in LST) and start to breakdown. This process corresponds to the start of the transition region. As the transition process develops, the u_{RMS} values increase due to the higher occurrence of turbulent spots, and finally settle to a new level once the fully turbulent regime is attained. The velocity fluctuations were measured using streamwise hotwire traverses at a constant height of 300 μm from the flat plate's surface. At this location, the hotwire probe was placed around the maximum of the streamwise velocity fluctuations' profile, which would allow for greater sensitivity to the detect the onset of transition. Based on this approach, the transition location uncertainty was determined to be $\pm$ 15 mm. The transition Reynolds numbers for all suction cases in the smooth configuration are summarized in Table 1. For all cases with suction turned on, the transition position was delayed with respect to the *no suction* configuration, with C1/0.400 being slightly less effective in terms of transition delay than C3,5/0.200 and *full suction*.

This difference can mainly be attributed to more or less better matching between the streamwise spatial evolution of the TS instabilities and the suction distribution. Consequently, C1/0.400, despite having the largest local suction velocity, does not apply suction at a streamwise location that will most effectively stabilize the TS instability, as opposed to the C3,5/0.200 or *full suction* cases. The first row in Table 1 refers to the transition position over the solid wall panel, and is provided to show the destabilizing effect of the porous wall without suction on the boundary layer. This effect is related to the wall impedance, and is discussed in further details in Rouviere et al (2021).

Table 1 Transition positions for all suction configurations over the solid wall ($p = 0\%$) and the suction panel ($p = 0.26\%$)

	suction case	Re_{xT} [-]	x_T [mm]
$p = 0\%$	*no suction*	1.92	740
$p = 0.26\%$	*no suction*	1.66	640
	C1/0.400	2.20	850
	C3,5/0.200	2.30	880
	full suction	2.30	880

2.3 Surface defect geometry and installation

In the first part of this experimental campaign (presented in Methel et al (2019)), wires were tested as surface defects. Although not generally found on aerodynamic surfaces, this type of defect was mainly chosen as a proof-of-concept because of its ease of installation and limited degrees of freedom. In an attempt to investigate more representative defects, FFS and gaps were then studied, and are presented here. Although idealized shapes, these two types of defects can model the junction between two panels, and of particular interest in the present case, between suction and solid panels. As a note, due to the flat plate model constraints, backward-facing steps could not be tested.

Tables 2 and 3 provide local boundary layer dimensions and the geometry of selected FFS and gaps that will be discussed in detail in the following sections. Also included, are all the critical defects (at which transition occurs at the defect location), which, as will be discussed in more details later are critical regardless of the application or not of wall suction. Additionally, any defect that has its transition location further downstream from its position is defined as subcritical.

For the FFS, h corresponds to the step height, while for the gap, h is the depth and b the width (in the streamwise direction). In the z-direction, the defect's spanwise dimension is assumed to be "infinitely" large compared to the other two directions, such that defects can be considered two-dimensional. In both tables, the selected defects mounted at x equal to 640 mm correspond to the location at the downstream junction of the suction panel with the flat plate, also shown in Figure 2. Additional defect locations were chosen within the suction region: FFS were mounted at x equal to 430 mm, the junction between chambers 5 and 6 (thereby making suction inoperative of the last four suction chambers); while gaps were mounted at x equal to 360 mm, within the region of chamber 4. The difference is x position between these two additional defect locations is due to internal geometric features of the flat plate that did not allow to match the gap position to the already-tested FFS.

To enable comparison, all defects dimensions were normalized with respect to the same length scale: the local boundary layer displacement thickness δ_1 in the corresponding smooth configuration. This δ_1 value was calculated using a boundary layer code, solving the parabolic Prandtl equation using experimental measurements as the boundary conditions for the external velocity distributions. The result from these calculations is shown in Tables 2 and 3 for each suction configuration to account for the slight change in boundary layer

thickness due to suction. Relatively good agreement between calculated and experimental displacement thicknesses were found; however, since experimental uncertainty on integral boundary layer parameters can be high, calculated values were used instead. Note that only one column is used for both the *full suction* and C3,5/0.200 cases: downstream of the suction region, at x equal to 640 mm, calculated boundary layer thicknesses were identical for these two cases. However, over the suction region at x equal to 430 mm, the local effect of wall suction is significant, and C3,5/0.200 and *full suction* have different δ_1 values.

Once a defect was mounted, its position remained fixed, and h/δ_1 and b/δ_1 values in the tables are therefore given for each suction configuration. The FFS are then referred to using the average $\sim h/\delta_1$ value provided in the table. On the other hand, due to the two parameters, gaps are referred to using their label, which gives the depth and width dimensions. A full list of all tested FFS and gaps is given in the Appendix.

Table 2 Selected FFS geometry (Asterisk corresponds to critical FFS, for which transition occurs immediately downstream

		no suction	C1/0.400	C3,5/0.200 ***(full suction)***	
		x = 640 mm (N = 5.53)			
	δ_1 (3C3D) [µm]	840	820	800	
Label	FFS h [µm]	h/δ_1			$\sim h/\delta_1$
FFS-650µm-640	650	0.77	0.79	0.81	∼0.8
FFS-850µm-640	850	1.01	1.04	1.06	∼1.0
FFS-1050µm-640*	1050	1.25	1.28	1.31	∼1.3
FFS-1150µm-640*	1150	1.37	1.40	1.44	∼1.4
		x = 430 mm (N = 3.94)			
	δ_1 (3C3D) [µm]	700	670	620 (***660***)	
Label	FFS h [µm]	h/δ_1			$\sim h/\delta_1$
FFS-1050µm-430*	1050	1.5	1.57	1.72 (***1.59***)	∼1.6

The FFS consisted of plastic shims of varying thicknesses with square edges that were adhered to the flat plate surface. The height of the FFS was then measured at the junction between the flat plate and the shim using Heidenhain LS388 linear encoders that have an accuracy to within 5 µm. However, repeatability tests for installation and height measurements indicated an uncertainty closer to ±25 µm for the given FFS heights.

For the gap at the junction between the suction region and the flat plate, a groove was incised, in which the gap insert could slide in. For the one inside the suction region, a support for the gap insert was mounted to the floor of chamber 4, the insert slid in, and the sealing suction panel was drilled to allow the insert to come through. In both configurations, verification that the inserts were flush-mounted was performed using the linear encoders. All gap inserts were 3D-printed in plastic and dimensions were verified using a depth gauge: width was measured before installation and depth *in situ*.

Table 3 Selected gaps dimensions. (Asterisk corresponds to critical gap, for which transition occurs immediately downstream

.)

				no suction		C1/0.400		C3,5/0.200 (***full suction***)	
				$x = 640$ mm ($N = 5.53$)					
		δ_1 (3C3D) [µm]		840		820		800	
Label	h [mm]	b [mm]	b/h	h/δ_1	b/δ_1	h/δ_1	b/δ_1	h/δ_1	b/δ_1
GAP-1200µm-8mm	1.2	8	6.7	1.4	9.5	1.5	9.8	1.5	10
GAP-1200µm-20mm*	1.2	20	16.7	1.4	23.8	1.5	24.4	1.5	25
GAP-15000µm-12mm*	15	12	0.8	17.9	14.3	18.3	14.6	18.75	15
				$x = 360$ mm ($N = 3.35$)					
		δ_1 (3C3D) [µm]		631		600		590 (***610***)	
Label	h [mm]	b [mm]	b/h	h/δ_1	b/δ_1	h/δ_1	b/δ_1	h/δ_1	b/δ_1
GAP-1200µm-18mm*	1.2	18	15	1.9	28.6	2.0	30.0	2.0 (***2.0***)	30.5 (***29.5***)

3 Effects of wall suction with FFS and gaps on boundary layer transition

In this section, the effects of wall suction combined with either FFS or gaps on boundary layer transition are discussed. The following two subsections experimentally characterize the combined effect of suction with FFS or gaps respectively, in terms of mean flow modifications, transition positions, and transition mechanisms. Finally, the last section uses linear stability theory to determine the ΔN for FFS and gaps in all suction configurations.

3.1 Combined FFS and wall suction

In this section, the combined effect of FFS and wall suction will be investigated through three main aspects: modification of the transition location, evolution of the boundary layer profiles, and identification of the transition mechanisms through frequency analysis of the instabilities developing in the laminar region. The effect of FFS can first be observed in terms of transition position, as shown in Figure 5. Figure 5(a) shows the transition location in terms of Reynolds number relative to the global reference frame. All the transition Reynolds numbers are given as a function of the tested FFS relative height, h/δ_1, and results from Wang and Gaster (2005). In general, as the FFS relative height increases, the transition Reynolds number decreases. However comparison between data sets is difficult because transition Reynolds number seems to be bounded by two limits. The upper limit, where h/δ_1 equal to zero (the smooth case), is determined either by the freestream turbulence level or the suction configuration. The lower limit is determined by the various positions of the surface defects that fix the transition position once critical dimensions are reached and **is shown as the dashed and dotted lines**. Additionally, since the transition position for the smooth case with *no suction* is already at 640 mm, no combination of *no suction* with an FFS at x equal to 640 mm was possible.

To allow some comparison, the effects of these two particular test facility-related parameters (smooth case transition position and FFS location) are removed using the non-dimensional transition parameter Δ_{xT}, defined as:

$$\Delta_{xT} = \frac{Re_{xT,SD} - Re_{x,SD}}{Re_{xT,noSD} - Re_{x,SD}}. \quad (1)$$

This Δ_{xT} parameter enables the comparison between different suction configurations and surface defect dimensions and locations. In this definition, $Re_{xT,SD}$ corresponds to the transition Reynolds number in the presence of a surface defect (SD), $Re_{xT,noSD}$ to that in the smooth configuration, and $Re_{x,SD}$ to the defect position.

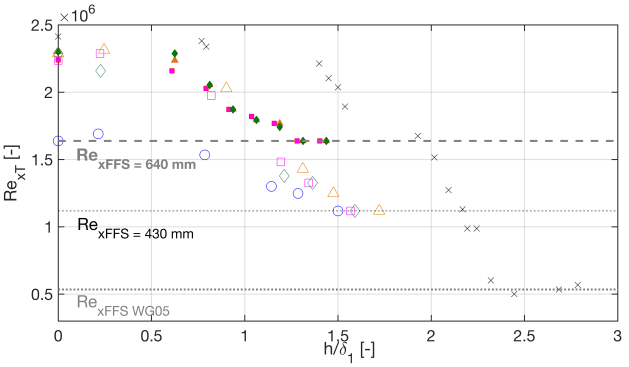

(a) Re_{xT} vs relative height h/δ_1 for FFS.

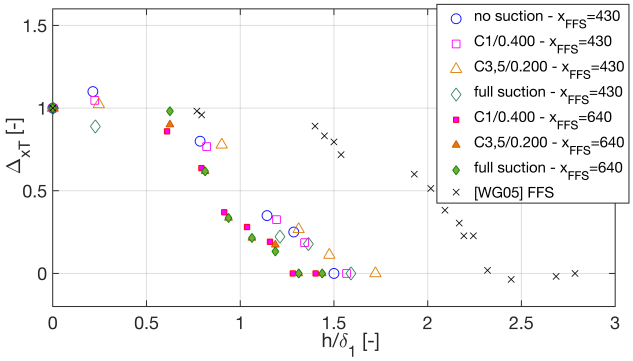

(b) Δ_{xT} vs height h/δ_1 for FFS.

Fig. 5 Variations in transition locations for all tested FFS. Suction configurations with solid symbols indicate FFS at x = 430 mm and with hollow symbols FFS at x = 640 mm. Grey-dash and black-dotted lines indicating the FFS position in terms of Reynolds number. Similar for Wang and Gaster (2005) data, with transition positions given with black crosses and the FFS position by the grey-dotted line.

For values of Δ_{xT} equal to 1, transition position is equivalent to the one in the smooth configuration, while for values equal to 0, transition is located at

the defect position, and the defect is considered "critical". In particular, the critical dimensions will be defined as the minimum values starting at which transition occurs immediately downstream of the defect.

Figure 5(b) thus shows the Δ_{xT} parameter as a function of FFS relative height. As a note, cases with Δ_{xT} greater than one correspond to cases with surface defects that have transition positions upstream of the smooth case, but within measurement uncertainty. From the figure, data from the present study generally cluster around a trendline, which indicates a critical FFS relative height approximately equal to 1.3. However, the use of the Δ_{xT} parameter does not allow to overlay the present data set with the one from Wang and Gaster (2005), where the critical h/δ_1 is closer to 2.5. This difference seems to indicate that the Δ_{xT} parameter does not include all the parameters to determine a universal critical value.

One of the more appreciable difference between the two studies could be attributed to the wind tunnel facilities used, which has different levels of freestream turbulence. In their publication, Wang and Gaster show that in the smooth case, the transition N factor is equal to 7.4. Based on Mack's relation (Mack (1977)), the corresponding freestream turbulence level of this facility is approximately 0.14%. As a reminder, the turbulence level for the present facility at the nominal operating point is 0.18%. Based on this difference, boundary layers developing in freestream flows with lower turbulence levels seem to allow for greater critical FFS h/δ_1.

Figure 6 next shows the local response of the mean velocity profiles to the surface defects. A Blasius profile is included to provide a reference to which the experimental profiles can be compared. The mean velocity profiles for different FFS relative heights shown in Figure 6 are for the *full suction* configuration only, but are representative of all suction configurations, including *no suction*. In other words, the shape of the mean velocity profile in the immediate vicinity of the FFS is dominated by the defect rather than by the effect of wall suction. Upstream of the FFS, Figure 6(a) shows that as the step's relative height increases, so does that height of the mean velocity profiles's inflection point. However, downstream of the step (Figures 6(b) and 6(c)), profiles do not show significant differences, even in the case of the critical FFS.

Further understanding of the transition mechanisms involved in the combined presence of FFS and the different suction configurations can be provided through unsteady data analysis. As mentioned in the overview of the reference configuration, the transition mechanism in the present investigation is primarily governed by the linear amplification of TS instabilities. Based on LST, the TS instabilities with frequency close to 600 Hz are responsible for transition.

This theoretical result is confirmed experimentally through spectral analysis of the streamwise velocity fluctuations inside the boundary layer upstream to the transition position. Figure 7 shows the power spectral densities (PSD) at 300 µm from the wall for a subcritical and critical FFS. Across all configurations, a bulge ranging from 400 Hz to 800 Hz corresponds to the frequencies

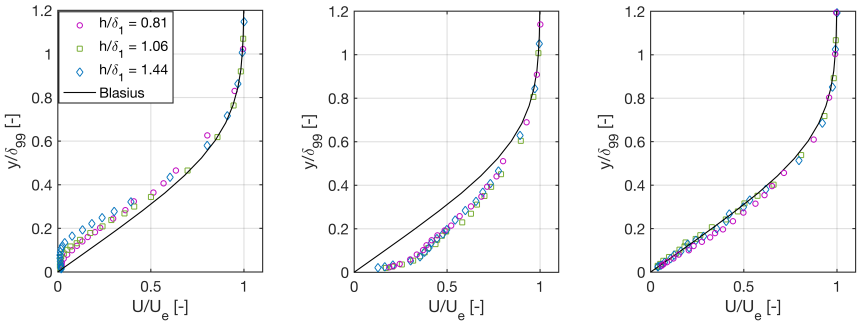

(a) x = x_{FFS} - 4 mm (b) x = x_{FFS} + 1 mm (c) x = x_{FFS} + 10 mm

Fig. 6 Evolution of the mean velocity profiles in the FFS region (x_{FFS} = 640 mm) for different FFS heights for the *full suction* configuration.

of the amplified TS instabilities. This observation is characteristic of all spectra for the tested FFS, which indicates that, for both subcritical and critical FFS, laminar-turbulent transition is still driven by TS instabilities. As a note, the visible peak at 290 Hz is Reynolds number independent and does not correspond to any harmonic of the rotational speed of the driving fan. To the best of the authors knowledge, this perturbation is attributed to an acoustic perturbation inside the wind tunnel.

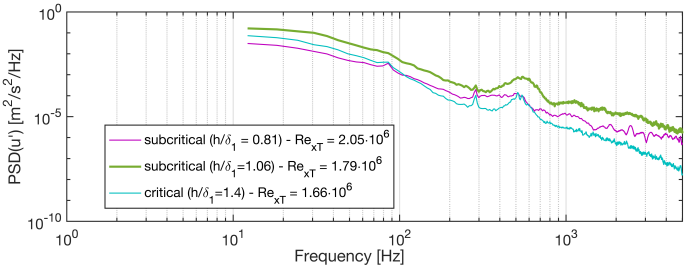

Fig. 7 PSD of streamwise velocity fluctuations u' (probed at y = 300µm from wall) at the transition Reynolds number for selected subcritical and critical FFS for *full suction*.

Streamwise velocity fluctuations *u'* profiles were then evaluated over the narrow band of frequencies that were most amplified for each type of surface defect. Figure 8 compares the effect of suction and step height at upstream (x = 608 mm) and downstream (x = 650 mm) locations from the step for *u'* profiles evaluated over [592-632] Hz. This figure also illustrates the competing effects occurring over the same TS instabilities between the attenuation from wall suction and the increased amplification from the FFS.

In Figure 8(a), the amplification due to the subcritical FFS with h/δ_1 equal to 0.6 seems to be relatively the same for the cases with suction: across the step, amplitudes are approximately multiplied by 3, which could also be expressed

as an amplification of approximately e^1. However, the effectiveness of wall suction in attenuating instabilities is clearly visible since even downstream of the step, the profiles with suction are still an order of magnitude lower than the *no suction* profile upstream of the step. Finally, all profiles have a shape close to that of a TS profile, even though in the *no suction* case, the boundary layer is already undergoing transition.

For a larger but still subcritical step height, shown in Figure 8(b), the resulting amplification is greater than that resulting from the smaller step in Figure 8(a). In this case, *u'* profiles approximately increased ten-fold. Additionally, the step also starts to influence upstream *u'* profiles, most noticeably in the *no suction* case. Although well upstream of the recirculation region, the *no suction* profile at x equal to 608 mm is disrupted by the presence of the step, as shown by the additional local maximum in the near wall region. This second maximum has a lower amplitude than the principal maximum that is located at a higher altitude inside the profile.

Finally, in the critical case from Figure 8(c), the effects mentioned for the previous step height are even further exacerbated. Across the step, the profiles with suction now undergo an amplification close to twenty-fold. The upstream influence of the step on the profiles is also more pronounced for this larger h/δ_1 value: for example, in the *no suction* configuration, the two maxima are almost equal. The presence of these two maxima from the step's upstream influence can also be seen for the cases with suction by the modulation of the two profiles in the inset graph.

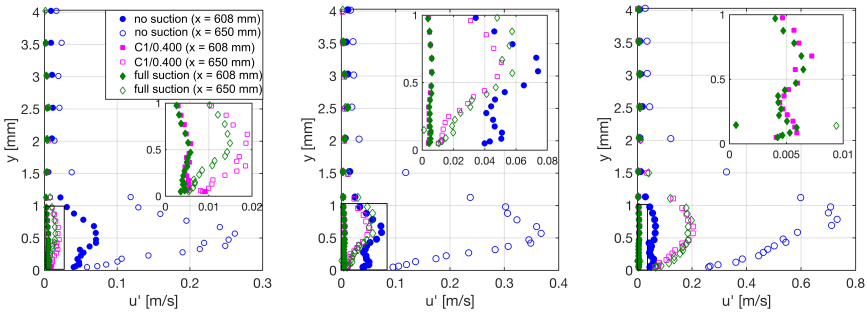

(a) h/δ_1 ∼0.8 (b) h/δ_1 ∼1.0 (c) h/δ_1 ∼1.4 (crit)

Fig. 8 Evolution of *u'* profiles (evaluated over [592-632] Hz) between streamwise positions x = 608 mm and x = 650 mm for different FFS heights and suction configurations (x_{FFS} = 640 mm).

Overall, although unable to change the critical FFS height, wall suction in the presence of subcritical FFS is still an effective method to delay transition, with respect to the equivalent no suction case.

3.2 Combined gaps and wall suction

Following the same structure as the previous section, the effects of gaps combined with wall suction will be investigated through transition positions, boundary layer profiles and power spectral densities plots.

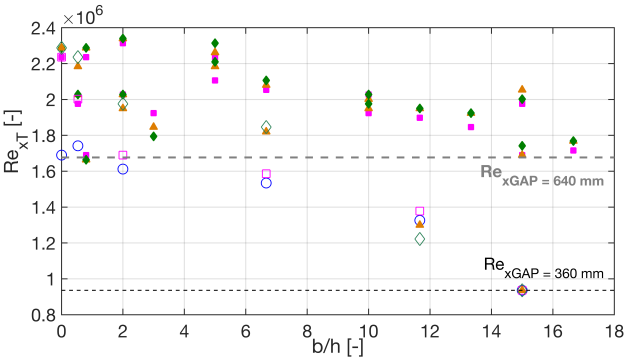

(a) $\mathrm{Re_{xT}}$ vs aspect ratio b/h for gaps.

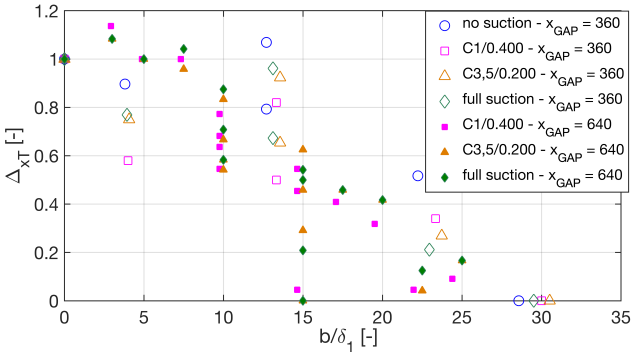

(b) Δ_{xT} vs width b/δ_1 for gaps.

Fig. 9 Variations in transition locations for all tested gaps as a function of aspect ratio b/h or width b/δ_1. Suction configurations with solid symbols indicate gaps at $x = 360$ mm and with hollow symbols gaps at $x = 640$ mm. Dash and dotted lines indicating the gaps' position in terms of Reynolds number.

Figure 9 shows the evolution of the transition position for all tested gaps, both in terms of Reynolds number and the criterion Δ_{xT}(equal to 1 in the case of a smooth-wall transition and 0 in the presence of a critical defect). Note that Figure 9(a) shows the transition Reynolds number as a function of the gaps' aspect ratio b/h, while Figure 9(b) is the Δ_{xT} parameter as a function of the relative width b/δ_1. These two graphs are used to highlight that, for the range of b/h presently tested, width is the driving parameter that affects boundary layer stability. This finding is in agreement with previous studies,

such as Forte et al (2015) where depth was found to have a minimal impact for b/h values greater than 5.

In general, Figure 9(a) shows that increasing b/h tends to move the transition position upstream; however, this trend is not so obvious at the extremes, i.e., for deep gaps (here, $b/h < 1$) or shallow gaps (here, $b/h > 12$). Some explanations for this lack of trend could be that in one case, deep gaps can start to act as resonators (Sarohia (1977) and Rossiter (1964)) and have complex flow patters (Sinha et al (1982)), while wide gaps can act more akin to a combination of a backward- and forward-facing step.

As summarized in Table 3, the three critical gaps that were tested established conjunct critical criteria of: $h/\delta_1 \geq 1.4$ and $b/\delta_1 \geq 14$. These values are slightly smaller than criteria established by Olive and Blanchard (1982) (and later confirmed by the studies summarized in Béguet et al (2016)) who found critical values of $h/\delta_1 \geq 2$ and $b/\delta_1 \geq 18$. Although generally of the same order of magnitude, the slightly more stable behavior of the boundary layers for these previous experiments could be attributed to two main factors: first, some of these investigations were performed on ONERA-D airfoils, i.e., with pressure gradients; and, second, the gaps were introduced much further upstream from the smooth case transition position than in the present study.

Figure 10 then shows the streamwise evolution of mean velocity profiles for three suction configurations over the critical gap GAP-1200µm-20mm. Upstream of the gap, the *full suction* profile is slightly fuller than the other suction configurations due to the local action of wall suction. However, inside and downstream of the gap, differences between the suction configurations disappear as boundary layer profiles overlap.

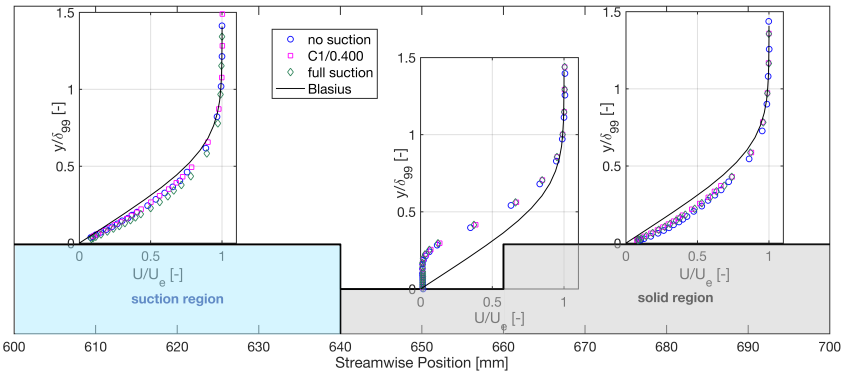

Fig. 10 Evolution of the mean velocity profiles over critical gap GAP-1200 µm-20 mm ($x_{\mathrm{GAP}} = 640$ mm).

Since differences between the suction configurations or critical surface defects are not discernible using the mean velocity profiles, further analysis using unsteady data is necessary to investigate how transition mechanisms are

affected. Similar to the previous section, Figure 11 shows the power spectral densities (PSD) at 300 µm from the wall for a subcritical and a critical gap at the transition position. For both cases, a bulge over frequencies between 400 Hz and 800 Hz can be identified and related to the amplified TS instabilities.

However, a second bulge over frequencies from 1 kHz to 3 kHz is also observed for both critical gaps (thick green and black curves), and can actually be related to an inflection point instability, similar to the transition mechanism induced by a critical wire, as was shown in Methel et al (2019). Referring to Figure 10, the mean velocity profiles inside the gap all exhibit the inflection point (at the same height as the gap lip), which is responsible for the amplification of high frequency instabilities. For the critical gap with $h/\delta_1 = 1.5$ and $b/\delta_1 = 25$, both the TS and inflection-point instabilities have comparable amplitudes, which seems to indicate that both types of mechanisms could be contributing to the onset of transition. The competition between the two transition mechanisms is even more apparent for the critical gap with $h/\delta_1 = 2$ and $b/\delta_1 = 30$, where the high frequency bulge has greater amplitude than that of the TS instabilities. Therefore, to allow for comparisons between all different configurations, only TS instabilities will be investigated in the remainder of this section.

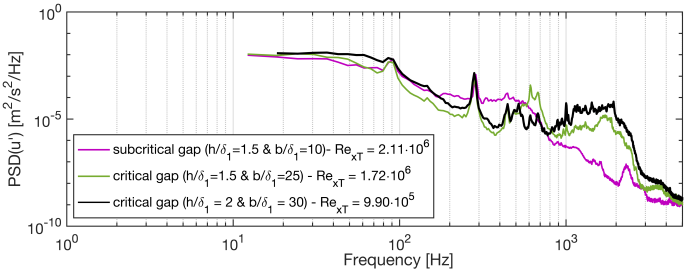

Fig. 11 PSD of streamwise velocity fluctuations u' (probed at y = 300µm from wall) at the transition Reynolds number for selected subcritical and critical gaps for *full suction*.

Figure 12 shows the evolution of streamwise velocity fluctuation profiles over the narrow range of 500 Hz to 540 Hz for the subcritical gap with streamwise width of 1200 µm and depth of 8 mm. Competition between the stabilizing wall suction and the destabilizing defect is observed across this gap. Upstream (Figure 12(a)) and downstream (Figure 12(b)) of the gap, all configurations with suction overlap relatively closely, and have significantly lower amplitudes than the *no suction* configuration. In particular, *no suction* experiences greater amplification (approximately five-fold), as opposed to the cases with suction that have their amplitudes approximately tripled.

Further downstream (Figure 12(c)), as expected from its earlier transition in the smooth configuration reported in Table 1, the C1/0.400 case starts to amplify faster than either C3,5/0.200 or *full suction*. Note that at x equal to 750 mm, the suction configurations have amplitudes that are of the same

order of magnitude as the *no suction* profile over x equal to 608 mm. Across all streamwise positions, the u' profiles also maintain a shape similar to that of a TS profile.

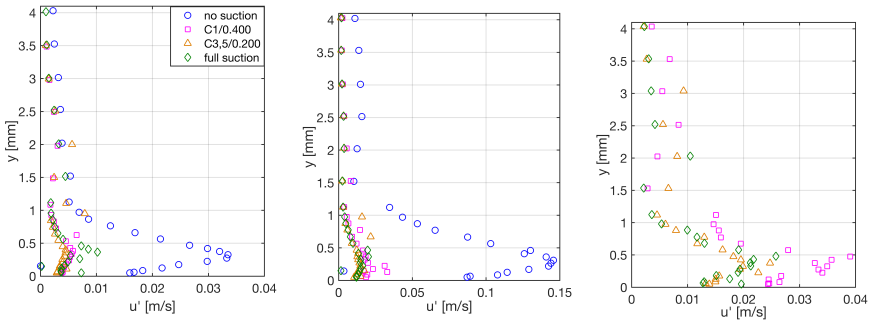

(a) $x = 608$ mm (b) $x = 650$ mm (c) $x = 750$ mm

Fig. 12 Evolution of u' profiles (evaluated over [592-632] Hz) for GAP-1200µm-8mm and all suction configurations ($x_{\mathrm{GAP}} = 640$ mm). The *no suction* configuration is removed after transition occurs.

3.3 Intermediate summary

Based on findings in the current and previous sections, all subcritical FFS and gaps were found to precipitate the onset of transition by further amplifying the existing primary modes of the boundary layer. Consequently, wall suction, which works to attenuate these same viscous instabilities, can effectively compete with these subcritical defects and therefore reduce their destabilizing effect. However, wall suction at the chosen levels was not effective enough to modify the relative dimensions of the critical FFS or gaps. Values of $h/\delta_1 \geq 1.3$ were found for the critical FFS, whereas the conjunct critical dimensions for depth and width of $h/\delta_1 \geq 1.4$, and $b/\delta_1 \geq 14$ respectively were found for the critical gaps. In these critical cases, regardless of whether the transition mechanism could be attributed to the TS or inflection-point instabilities, the increase in amplification was too significant to be offset by wall suction, given the selected flow rates.

Once the combined effect of wall suction with subcritical FFS and gaps was found to act on the same instabilities, the use of LST was rationalized, as will be discussed in the following section.

4 Modeling using the ΔN method

One approach to modeling the additional amplification or attenuation of instabilities through external factors (here surface defects and wall suction) is by modifying the maximum N factor envelope curve predicted using LST.

In the present investigation, numerical boundary layer profiles were calculated at various streamwise positions by solving Prandtl's boundary layer equations, using ONERA's in-house code 3C3D. Input to this code include the experimental pressure coefficient or freestream velocity. Additionally, a normal velocity can be imposed at the wall to replicate the effects of wall suction on the boundary layer. The normal velocity V_p is estimated by solving for the velocity in the mass flow rate equation such that:

$$V_p = \frac{\dot{m}}{\rho A_{\text{suction area}}} \tag{2}$$

For C1/0.400 for example, since $A_{\text{suction area}}$ is the area of the first suction chamber (350 mm by 50 mm), $\dot{m}$ is equal to 0.4 g.s^{-1}, and ρ the density of air to 1.2 kg.m^{-3}, V_p is approximately 0.02 m.s^{-1}. Next the numerical boundary layer profiles are input into ONERA's in-house LST code CASTET, which solves the Orr-Sommerfeld equation, to obtain local stability information.

The first step consists in determining the maximum N factor envelope curve for the smooth case for all suction configurations, such as the one shown in Figure 4 for *no suction*. For each smooth suction configuration, the transition N factor for this case is $N_{T,\text{smooth}}$. Next, using each envelope curve, the N factor at the transition position with a surface defect (SD) $N_{xT,\text{SD}}$ is evaluated. The difference

$$\Delta N = N_{T,\text{smooth}} - N_{xT,\text{SD}} \tag{3}$$

then provides a measure of the added amplification induced by the surface defect.

Figure 13 compares the ΔN for all subcritical suction configurations and FFS positions as a function of the relative height h/δ_1. Additionally, data from Wang and Gaster (2005) ([WG05]) and the model from Crouch et al (2006) ([CKN06]) are included to enable comparison with the closest configuration tested in the present study, *no suction*, labeled "ns x_{FFS}=430" on the figure.

Over the range of h/δ_1 shown, relatively good agreement is found between the model and the present data set. In general, the open symbols, which correspond to configurations where the FFS was located at the furthest streamwise location (the junction between the suction and solid regions) can be described with the [CKN06] model. However, for large values of h/δ_1 (i.e., close to the critical threshold of $h/\delta_1 \sim 1.3$) achieved with surface defects closer to the leading edge and for suction configurations C1/0.400 and C3,5/0.200, the obtained values of ΔN are greater than those predicted by the model. At this FFS position, located at the junction between the C5 and C6 chambers, the C1/0.400 and C3,5/0.200 configurations have fully provided their attenuation. The corresponding TS instabilities therefore have lower N factors compared to those of *no suction* or *full suction* at this same location.

Therefore, the current ΔN model, developed based on experiments without suction, is suitable for configurations with suction for subcritical FFS heights; however, further improvements to the model could be considered for the h/δ_1 values greater than one in the presence of wall suction. In particular, the

fact that the sensitivity of the ΔN to h/δ_1 is increased for various suction distributions further supports the possibility of extending current models.

In general, the data from Wang and Gaster (where the critical h/δ_1 was $\sim$2.3) agree relatively well with the [CKN06] model, which is conservative (data from configurations with both adverse and favorable pressure gradients were used for its development) up to values of h/δ_1 approximately equal to 2. Beyond this threshold, the relationship between ΔN and h/δ_1 for Wang's experimental data cannot easily be modeled by a single linear equation.

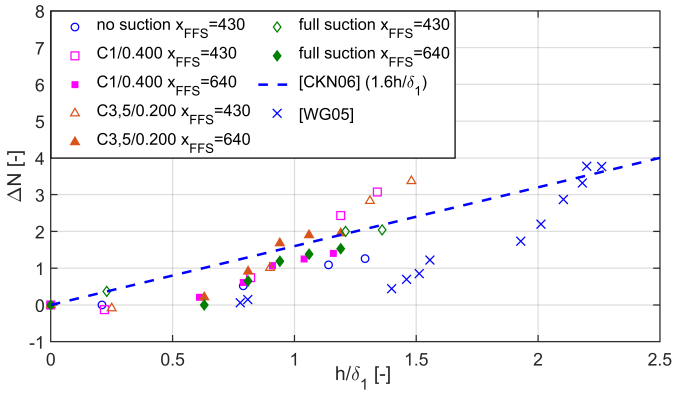

Fig. 13 ΔN for all subcritical suction configurations with FFS compared with model for FFS from Crouch et al (2006) and with measurements from Wang and Gaster (2005).

Next, Figure 14 shows the evolution of the ΔN values for all subcritical gaps at both positions as a function of the relative width b/δ_1. In general, as b/δ_1 increases, so does ΔN. Additionally, and similar to the FFS, configurations with suction seem to be more sensitive (i.e., have larger ΔN values) than the *no suction* configuration.

Additionally, the model developed in Crouch et al (2020) for the deep gaps, and labeled [CKS20], is also provided on Figure 14. Only the deep gap model proposed by the authors is used since all of the gaps considered in the present study have $b/h < 36$ (written otherwise as $h/b > 0.028$). This latest model agrees relatively well with the present data. In particular, the model can be considered a conservative estimate for the *no suction* case (a porous wall with no passive or active suction), which is closest to the solid wall case that was used to developed the model. More generally, agreement between the model and the present data is best for the gaps located furthest downstream (at streamwise location $x = 640$ mm from the leading edge), regardless of the suction configuration.

In general, ΔN models for different types of surface defects are generated semi-empirically by combining measurement and LST calculations. The current data sets therefore provide experimental validation to the currently existing models, showing that both the general ΔN approach, and more particularly the models for the FFS and the gaps, can still applied in the presence of

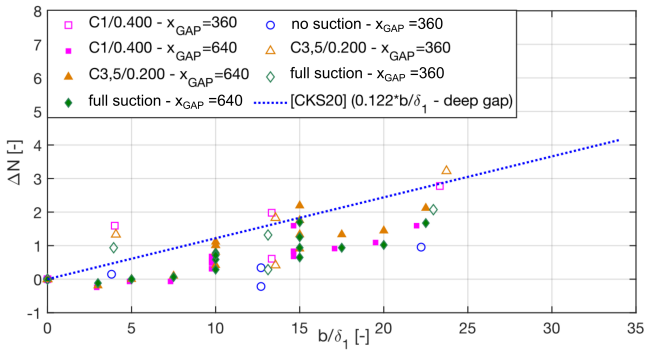

Fig. 14 ΔN for all subcritical suction configurations with gaps compared with the model from Crouch et al (2020).

wall suction. These results can therefore be used during the design of aerodynamics surfaces with wall suction to define tolerances for both manufacturing and assembly.

5 Conclusion

An experimental investigation on the effects of FFS and gaps on laminar-turbulent transition of a boundary layer undergoing wall suction was performed. For both types of surface defects, wall suction at the chosen flow rates was unable to modify the critical defect dimensions (above which transition occurs immediately downstream of the defect location), regardless of the suction distributions. On one hand, this finding indicates that the local reduction in boundary layer thickness, induced by suction, is therefore not significant enough to influence transition criteria. On the other hand, the destabilizing effect induced by critical defects can also be seen as too strong and sudden for wall suction to be effective. The critical relative height h/δ_1 for the FFS was approximately 1.3, and the conjunct critical relative depth h/δ_1 and relative width b/δ_1 were 1.4 and 14 respectively for the gaps.

However, in the presence of subcritical FFS and gaps, wall suction did exhibit robustness by still delaying transition with respect to the *no suction* configuration, albeit less effectively than in the smooth case. This effect is due to the fact that neither subcritical FFS and gaps nor suction fundamentally change the transition mechanism; thus, all compete over the same viscous instabilities. The relatively high critical dimensions and the unmodified transition mechanism warranted the use of the ΔN method to capture the gradual decrease in effectiveness of wall suction in transition delay. For low subcritical defect dimensions, existing conservative ΔN models developed for solid surfaces can adequately capture their effect combined to wall suction; however, as defect dimensions approach critical values, models will have to be modified

to account for the stronger ΔN shift induced by defects on a sucked boundary layer.

Although unable to annul or postpone the critical dimensions of either FFS or gaps at its selected flow rates, wall suction still proved to be an effective LFC technology in the presence of subcritical defects. This observation is in agreement with findings from the first part of this study found in Methel et al (2019). Moreover, numerical studies, such as by Zahn and Rist (2018), observed that, for suction flow rates much greater than those used in the present study, wall suction through a slot located immediately upstream of a step could prevent transition, with respect to the case without suction. Wall suction therefore does offer the ability to reduce the effect of surface imperfections. As manufacturing and assembly processes for aerodynamic surfaces improve, the resulting reduction in tolerances for surface defects could become a significant argument in favor of a more widespread implementation of wall suction on commercial aircraft.

Appendix A All tested FFS and gaps dimensions and positions

Table A1 Relative heights for FFS at streamwise position $x_{\mathrm{FFS}} = 430$ mm ($\mathrm{Re}_x = 1.12{\cdot}10^6$, junction between chambers C5 and C6). (Asterisks correspond to critical FFS.)

		$x_{\mathrm{FFS}} = 430$ mm				
		no suction	C1/0.400	C3,5/0.200	*full suction*	
	δ_1 (3C3D) [µm]	700	670	610	660	
Label	FFS h [µm]	h/δ_1				∼rounded h/δ_1
FFS-150µm-430	150	0.21	0.22	0.25	0.23	∼0.2
FFS-550µm-430	550	0.79	0.82	0.90	0.83	∼0.8
FFS-800µm-430	800	1.14	1.19	1.31	1.21	∼1.2
FFS-900µm-430	900	1.29	1.34	1.48	1.36	∼1.4
FFS-1050µm-430*	1050	1.5	1.57	1.72	1.59	∼1.6

Table A2 Relative heights for FFS at streamwise position $x_{\mathrm{FFS}} = 640$ mm ($\mathrm{Re}_x = 1.66{\cdot}10^6$, junction between the end of the suction region and flat plate). (Asterisks correspond to critical FFS.)

		$x_{\mathrm{FFS}} = 640$ mm				
		no suction	C1/0.400	C3,5/0.200	*full suction*	
	δ_1 (3C3D) [µm]	840	820	800	800	
Label	FFS h [µm]	h/δ_1				∼rounded h/δ_1
FFS-500µm-640	500	0.60	0.61	0.63	0.63	∼0.6
FFS-650µm-640	650	0.77	0.79	0.81	0.81	∼0.8
FFS-750µm-640	750	0.89	0.91	0.94	0.94	∼0.9
FFS-850µm-640	850	1.01	1.04	1.06	1.06	∼1.0
FFS-950µm-640	950	1.13	1.16	1.19	1.19	∼1.2
FFS-1050µm-640*	1050	1.25	1.28	1.31	1.31	∼1.3
FFS-1150µm-640*	1150	1.37	1.40	1.44	1.44	∼1.4

Table A3 All tested gap dimensions for $x_{\mathrm{GAP}} = 360$ mm. (Asterisks correspond to critical gaps.)

		no suction		C1/0.400		C3,5/0.200		*full suction*	
h/δ_1 (3C3D) [µm]		631		600		590		610	
Label	b/h	h/δ_1	b/δ_1	h/δ_1	b/δ_1	h/δ_1	b/δ_1	h/δ_1	b/δ_1
GAP-1200µm-2.4mm	2	1.9	3.8	2.0	4.0	2.0	4.1	2.0	3.9
GAP-1200µm-8mm	6.7	1.9	12.7	2.0	13.3	2.0	13.6	2.0	13.1
GAP-1200µm-14mm	11.7	1.9	22.2	2.0	23.3	2.0	23.7	2.0	23.0
GAP-1200µm-18mm*	15	1.9	28.6	2.0	30.0	2.0	30.5	2.0	29.5
GAP-15000µm-8 mm	0.5	23.8	12.7	25.0	13.3	25.4	13.6	24.6	13.1

Table A4 All tested gap dimensions for $x_{GAP} = 640$ mm. (Asterisks correspond to critical gaps.)

				no suction		C1/0.400		C3,5/0.200 *full suction*	
		δ_1 (3C3D) [µm]		840		820		800	
Label	h [mm]	b [mm]	b/h	h/δ_1	b/δ_1	h/δ_1	b/δ_1	h/δ_1	b/δ_1
GAP-400µm-14mm	0.4	14	35	0.5	16.7	0.5	17.1	0.5	17.5
GAP-800µm-8mm	0.8	8	10	1	9.5	1	9.8	1	10
GAP-800µm-12mm	0.8	12	15	1	14.3	1	14.6	1	15
GAP-800µm-14mm	0.8	14	17.5	1	16.7	1	17.1	1	17.5
GAP-1200µm-2.4mm	1.2	2.4	2	1.4	2.9	1.5	2.9	1.5	3
GAP-1200µm-6mm	1.2	6	5	1.4	7.1	1.5	7.3	1.5	7.5
GAP-1200µm-8mm	1.2	8	6.7	1.4	9.5	1.5	9.8	1.5	10
GAP-1200µm-12mm	1.2	12	10	1.4	14.3	1.5	14.6	1.5	15
GAP-1200µm-14mm	1.2	14	11.7	1.4	16.7	1.5	17.1	1.5	17.5
GAP-1200µm-16mm	1.2	16	13.3	1.4	19	1.5	19.5	1.5	20
GAP-1200µm-18mm	1.2	18	15	1.4	21.4	1.5	22	1.5	22.5
GAP-1200µm-20mm*	1.2	20	16.7	1.4	23.8	1.5	24.4	1.5	25
GAP-1600µm-8mm	1.6	8	5	1.9	9.5	2	9.8	2	10
GAP-2400µm-12mm	2.4	12	5	2.9	14.3	2.9	14.6	3	15
GAP-4000µm-8mm	4	8	2	4.8	9.5	4.9	9.8	5	10
GAP-4000µm-12mm	4	12	3	4.8	14.3	4.9	14.6	5	15
GAP-5000µm-4mm	5	4	0.8	6	4.8	6.1	4.9	6.25	5
GAP-8000µm-8mm	8	8	1	9.5	9.5	9.8	9.8	10	10
GAP-8000µm-12mm	8	12	1.5	9.5	14.3	9.8	14.6	10	15
GAP-15000µm-8mm	15	8	0.5	17.9	9.5	18.3	9.8	18.75	10
GAP-15000µm-12mm*	15	12	0.8	17.9	14.3	18.3	14.6	18.75	15

References

Al-Maaitah A, Nayfeh A, Ragab S (1989) Effect of suction on the stability of subsonic flows over smooth backward-facing steps. AIAA Journal 28(11):1916–1924. https://doi.org/10.2514/6.1989-983

Arnal D, Archambaud J (2008) Laminar-turbulent transition control: NLF, LFC, HLFC. Advances in Laminar–Turbulent Transition Modeling, AVT-151 RTO AVT/VKI

Béguet S, Perraud J, Forte M, et al (2016) Modeling of transverse gaps effects on boundary-layer transition. Journal of Aircraft 54(2):794–801. https://doi.org/10.2514/1.c033647

Braslow A (1999) A history of suction-type laminar flow control with emphasis on flight research. Monographs in Aerospace History 13

Bulgubure C, Arnal D (1992) Dassault Falcon 50 laminar flow flight demonstrator. In: DGLR/3AF/RAeS First European Forum on Laminar Flow, URL https://www.gbv.de/dms/tib-ub-hannover/126870276.pdf

Corelli Grappadelli M, Sattler S, Scholz P, et al (2021) Experimental investigations of boundary layer transition on a flat plate with suction. In: AIAA Scitech 2021 Forum, p 1452, https://doi.org/10.2514/6.2021-1452

Costantini M, Risius S, Klein C (2015) Experimental investigation of the effect of forward-facing steps on boundary layer transition. Procedia IUTAM 14:152–162. https://doi.org/10.1016/j.piutam.2015.03.036

Crouch J, Kosorygin V (2020) Surface step effects on boundary-layer transition dominated by tollmien–schlichting instability. AIAA Journal 58(7):2943–2950. https://doi.org/10.2514/1.J058518

Crouch J, Kosorygin V, Ng L (2006) Modeling the effects of steps on boundary-layer transition. In: IUTAM Symposium on Laminar-Turbulent Transition, Springer, pp 37–44, https://doi.org/10.1007/1-4020-4159-4_4

Crouch J, Kosorygin V, Sutanto M (2020) Modeling gap effects on transition dominated by tollmien-schlichting instability. In: AIAA Aviation 2020, AIAA, pp 1–48, https://doi.org/10.2514/6.2020-3075

Dovgal A, Kozlov V, Michalke A (1994) Laminar boundary layer separation: instability and associated phenomena. Progress in Aerospace Sciences 30(1):61–94. https://doi.org/10.1016/0376-0421(94)90003-5

Edelmann CA, Rist U (2015) Impact of forward-facing steps on laminar-turbulent transition in transonic flows. AIAA Journal 53(9):2504–2511. https://doi.org/10.2514/1.J053529

Forte M, Gentili L, Béguet S, et al (2015) Experimental and numerical study of the effect of gaps on the laminar-turbulent transition for two-dimensional incompressible boundary-layers. In: 50th 3AF International Conference on Applied Aerodynamics, https://doi.org/10.1016/j.piutam.2015.03.073

Fransson JH (2004) Leading edge design process using a commercial flow solver. Experiments in fluids 37(6):929–932. https://doi.org/10.1007/s00348-004-0858-3

Hahn M, Pfenninger W (1973) Prevention of transition over a backward step by suction. Journal of Aircraft 10(10):618–622. https://doi.org/10.2514/3.60269

Joslin R (1998) Overview of laminar flow control. Tech. rep., NASA/TP-1998-208705

Klebanoff P, Tidstrom K (1972) Mechanism by which a two-dimensional roughness element induces boundary-layer transition. The Physics of Fluids 15(7):1173–1188. https://doi.org/10.1063/1.1694065

Krishnan K, Bertram O, Seibel O (2017) Review of hybrid laminar flow control systems. Progress in Aerospace Sciences 93:24–52. https://doi.org/10.1016/j.paerosci.2017.05.005

Lüdeke H, Backhaus K (2018) Direct TS-wave simulation on a laminar wing-profile with forward-facing step. In: New Results in Numerical and Experimental Fluid Mechanics XI. Springer International Publishing, Cham, pp 275–284, https://doi.org/10.1007/978-3-319-64519-3_25

Mack L (1977) Transition and laminar instability. JPL Publication 77-15

Maddalon D (1991) Hybrid Laminar Flow Control flight research. Research and Technology, NASA, TM 4331:47

Methel J, Vermeersch O, Forte M, et al (2018) Experimental characterization of the laminar-turbulent transition of a sucked boundary layer due to surface defects in a two-dimensional incompressible flow. 2018 Flow Control Conference, AIAA AVIATION Forum AIAA2018-3214. https://doi.org/10.2514/6.2018-3214

Methel J, Forte M, Vermeersch O, et al (2019) An experimental study on the effects of two-dimensional positive surface defects on the laminar–turbulent transition of a sucked boundary layer. Experiments in Fluids 60(6):94. https://doi.org/10.1007/s00348-019-2741-2

Morkovin M, Reshotko E, Herbert T (1994) Transition in open flow systems-a reassessment. Bull Am Phys Soc 39:1882

Nenni J, Gluyas G (1966) Aerodynamic design and analysis of an LFC surface. Astronautics & Aeronautics 4(7):52

Olive M, Blanchard A (1982) Etude expérimentale du déclenchement de la transition par des cavités en écoulement incompressible. Tech. rep., CERT DERAT OA18/5007

Perraud J, Séraudie A, Reneaux J, et al (2005) Effect of 2D and 3D imperfections on laminar-turbulent transition. In: CEAS Katnet Conference on Key Aerodynamic Technologies

Reed H, Saric W, Arnal D (1996) Linear stability theory applied to boundary layers. Annual Review of Fluid Mechanics 28(1):389–428. https://doi.org/10.1146/annurev.fl.28.010196.002133

Reynolds G, Saric W (1986) Experiments on the stability of the flat-plate boundary layer with suction. AIAA Journal 24(2):202–207. https://doi.org/10.2514/3.9246

Rius-Vidales AF, Kotsonis M (2020) Influence of a forward-facing step surface irregularity on swept wing transition. AIAA Journal 58(12):5243–5253. https://doi.org/10.2514/1.J059566

Rizzetta D, Visbal M (2014) Numerical simulation of excrescence generated transition. AIAA Journal 52(2):385–397. https://doi.org/10.2514/1.j052530

Rossiter J (1964) Wind tunnel experiments on the flow over rectangular cavities at subsonic and transonic speeds. Tech. rep., Ministry of Aviation, Royal Aircraft Establishment

Rouviere A, Méry F, Methel J, et al (2021) Experimental and numerical study on wall impedance effects on Tollmien–Schlichting waves. AIAA Journal (in press) https://doi.org/10.2514/1.J060536

Saric W, Carpenter A, Reed H (2011) Passive control of transition in three-dimensional boundary layers, with emphasis on discrete roughness elements. Philosophical Transactions of the Royal Society A: Mathematical, Physical and Engineering Sciences 369(1940):1352–1364. https://doi.org/10.1098/rsta.2010.0368

Sarohia V (1977) Experimental investigation of oscillations in flows over shallow cavities. AIAA Journal 15(7):984–991. https://doi.org/10.2514/6.1976-182

Sinha S, Gupta A, Oberai M (1982) Laminar separating flow over backsteps and cavities. ii-cavities. AIAA journal 20(3):370–375. https://doi.org/10.2514/3.7918

Smith A, Gamberoni N (1956) Transition, pressure gradient and stability theory. Tech. rep., Douglas Aircraft Co. ES 26388

Studer G, Arnal D, Houdeville R, et al (2006) Laminar–turbulent transition in oscillating boundary layer: experimental and numerical analysis using continuous wavelet transform. Experiments in fluids 41(5):685–698. https://doi.org/10.1007/s00348-006-0190-1

Van Ingen J (1956) A suggested semi-empirical method for the calculation of the boundary layer transition region. Technische Hogeschool Delft, Vliegtuigbouwkunde, Rapport VTH-74

Wang Y, Gaster M (2005) Effect of surface steps on boundary layer transition. Experiments in Fluids 39(4):679–686. https://doi.org/10.1007/s00348-005-1011-7

Zahn J, Rist U (2018) Study about boundary-layer suction at a juncture for sustained laminar flow. In: New Results in Numerical and Experimental Fluid Mechanics XI. Springer, p 349–358, https://doi.org/10.1007/978-3-319-64519-3_32